Nuclear Instruments and Methods in Physics Research A 621 (2010) 595–604

Contents lists available at ScienceDirect

Nuclear Instruments and Methods in Physics Research A

journal homepage: www.elsevier.com/locate/nima

Time walk correction for TOF-PET detectors based on a monolithic scintillation crystal coupled to a photosensor array

R. Vinke [a,*], H. Löhner [a], D.R. Schaart [b], H.T. van Dam [b], S. Seifert [b], F.J. Beekman [b,c], P. Dendooven [a]

[a] Kernfysisch Versneller Instituut, University of Groningen, Zernikelaan 25, 9747 AA Groningen, The Netherlands
[b] Delft University of Technology, Mekelweg 15, 2629 JB Delft, The Netherlands
[c] University Medical Centre Utrecht, Heidelberglaan 100, 3584 CX Utrecht, The Netherlands

ARTICLE INFO

Article history:
Received 10 June 2009
Received in revised form
14 May 2010
Accepted 16 May 2010
Available online 25 May 2010

Keywords:
Positron emission tomography
Timing resolution
TOF-PET
Positioning algorithm

ABSTRACT

When optimizing the timing performance of a time-of-flight positron emission tomography (TOF-PET) detector based on a monolithic scintillation crystal coupled to a photosensor array, time walk as a function of annihilation photon interaction location inside the crystal needs to be considered. In order to determine the 3D spatial coordinates of the annihilation photon interaction location, a maximum likelihood estimation algorithm was developed, based on a detector characterization by a scan of a 511 keV photon beam across the front and one of the side surfaces of the crystal. The time walk effect was investigated using a 20 mm × 20 mm × 12 mm LYSO crystal coupled to a fast 4 × 4 multi-anode photomultiplier tube (MAPMT). In the plane parallel to the photosensor array, a spatial resolution of 2.4 mm FWHM is obtained. In the direction perpendicular to the MAPMT (depth-of-interaction, DOI), the resolution ranges from 2.3 mm FWHM near the MAPMT to 4 mm FWHM at a distance of 10 mm. These resolutions are uncorrected for the ~1 mm beam diameter. A coincidence timing resolution of 358 ps FWHM is obtained in coincidence with a BaF_2 detector. A time walk depending on the 3D annihilation photon interaction location is observed. Throughout the crystal, the time walk spans a range of 100 ps. Calibration of the time walk vs. interaction location allows an event-by-event correction of the time walk.

1. Introduction

Positron emission tomography (PET) detectors based on a monolithic scintillation crystal coupled to a photosensor array have the potential to increase PET system sensitivity compared to block detectors consisting of pixelated crystals [1,2]. Additionally, it has been shown that statistics-based positioning algorithms give excellent intrinsic spatial resolution for detectors based on these monolithic scintillation crystals [2–6], with depth-of-interaction (DOI) reconstruction capability [7].

It is well known that including time-of-flight (TOF) information in the image reconstruction process can significantly reduce the noise variance in the image [8,9], thereby effectively increasing the PET system sensitivity. In the optimization of the timing performance of a TOF-PET detector based on a monolithic scintillation crystal coupled to a photosensor array, time walk as a function of annihilation photon interaction location inside the crystal needs to be considered. This study focuses on this effect. In order to determine the 3D spatial coordinates of the annihilation photon interaction location, a maximum likelihood estimation algorithm was developed. The timing performance was studied in a coincidence setup with a BaF_2 detector, using digital time pickoff techniques on the timing signals. The time walk as function of the 3D position-of-interaction is then deduced and an event-by-event correction can be applied.

2. Materials and methods

2.1. Experimental setup

A schematic view of the setup is shown in Fig. 1. A monolithic polished LYSO crystal with dimensions 20 mm × 20 mm × 12 mm was coupled to a Hamamatsu position-sensitive H8711-03 4 × 4 multi-anode photomultiplier (MAPMT) using Sylgard® 527 dielectric gel as coupling material [10]. The MAPMT anode sizes are 4.2 mm × 4.2 mm and the center-to-center spacing is 4.5 mm. The crystal sides not facing the MAPMT were covered with a reflective PTFE based material (Spectralon® [11]) to maximize the light collection efficiency. The last dynode signal of the MAPMT contains the light intensity collected by each individual channel. This signal therefore served as the 'timing signal' for the monolithic

* Corresponding author. Tel.: +31 50 363 8851.
E-mail address: ruudvinke@gmail.com (R. Vinke).

0168-9002/$ - see front matter © 2010 Elsevier B.V. All rights reserved.
doi:10.1016/j.nima.2010.05.034

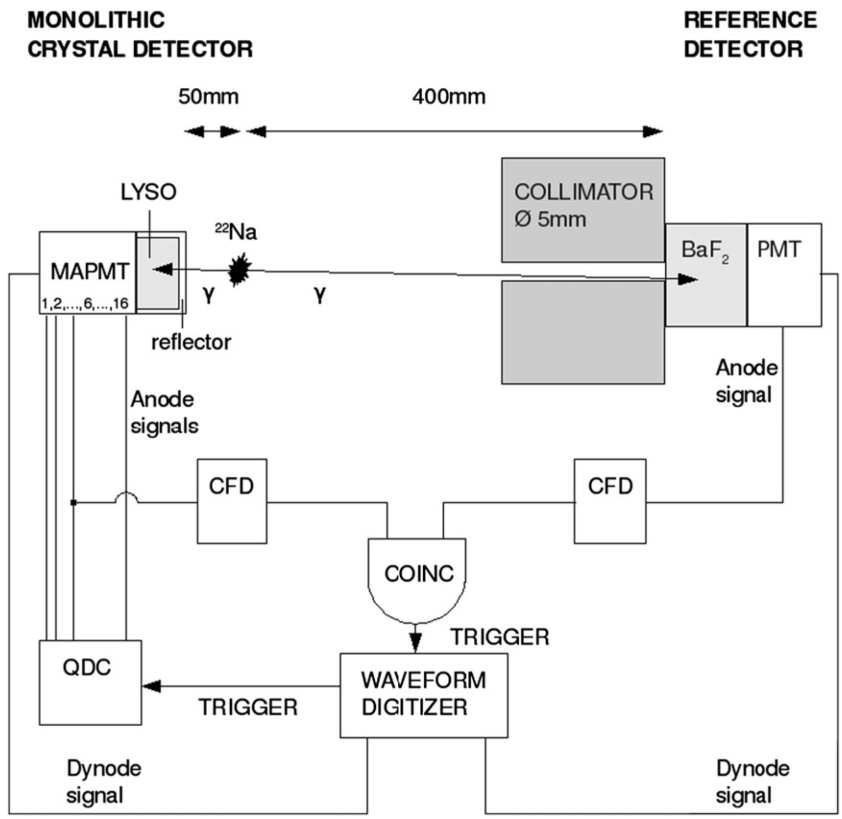

Fig. 1. Schematic view of the experimental setup.

crystal detector. A ^{22}Na source provided 511 keV positron annihilation photon pairs. A fast BaF_2 detector was used as a reference detector. This detector (Scionix model 25.4 B 20/2Q-BAF-X-NEG+VD29-124KT) consists of a 20 mm thick, 25.4 mm diameter crystal mounted on an XP2020Q photomultiplier tube and has a timing resolution for 511 keV photons of about 180 ps. The dynode (timing) signals of both detectors were sent to an Agilent DC282 waveform digitizer. No amplifiers were used. Timing traces were digitized at 2 GS/s (500 ps/pt) for both detectors at 2 GHz bandwidth. The MAPMT anode signals (the 'energy signals') were sent directly to a LeCroy 4300B 16-channel charge integrating ADC (QDC), interfaced to a CAMAC system. For deriving the coincidence trigger, one of the center anode signals of the MAPMT (anode #6) was split and one branch sent to a constant fraction discriminator (CFD). The anode output of the BaF_2 PMT was sent to a second CFD. The two CFD outputs were sent to a logic coincidence unit and the resulting output served as the trigger signal for the waveform digitizer.

The systems acquiring the energy and timing signals (the QDC and waveform digitizer, respectively,) were synchronized in order to be able to combine the energy and timing information for each event. This was done by operating the CAMAC system in 'slave'-mode: charge pulses were digitized only after a trigger was received from the waveform digitizer. A separate event counter was installed in the CAMAC system to count the number of triggers sent out by the waveform digitizer. In this way, events that were rejected by the QDC because they occurred during a 'dead time'-state could be tracked afterwards. Synchronization could be confirmed after acquisition by cross-correlating the energy of the MAPMT dynode pulse, as obtained from the waveform digitizer, with the sum of the MAPMT anode channels, as recorded by the CAMAC system. The synchronization of the waveform digitizer and CAMAC system leads to each event consisting of 2 digitized dynode pulses and the energies detected by the 16 anodes of the MAPMT.

To be able to reconstruct the 3D position-of-interaction of the gamma photons in the monolithic scintillation crystal (see Section 1), the detector response had to be calibrated as a function of gamma beam position. To obtain a beam with small spot size on the monolithic crystal, the ^{22}Na source was placed close to the monolithic crystal surface (50 mm). The reference detector was placed at a distance of 400 mm to the ^{22}Na source at the opposite side. By only taking coincidence events into account, the beam is electronically collimated at the monolithic crystal detector. The spot size of the gamma photon beam was 5 mm in diameter at the crystal surface of the reference detector (a 50 mm thick lead collimator with a 5 mm diameter hole was used for this purpose), resulting in a spot size of ~ 1 mm in diameter at the monolithic crystal surface whenever both photons of the annihilation pair were detected. Two perpendicular motorized translation stages allowed scanning the monolithic crystal in the plane perpendicular to the beam and obtain a position calibration set. A calibration scan of the front surface (XY-scan) was made. After this, the detector was turned by 90° and a calibration scan of one of the side surfaces (YZ-scan) was made. By combining the calibration information from these two directions, a 3D calibration set was obtained. This 3D calibration set was then used to estimate the 3D position-of-interaction of the gamma photons inside the crystal by Maximum Likelihood Estimation (MLE). Details are given in Sections 2.3 to 2.6. For the position analysis, only 511 keV photopeak events were taken into account for the monolithic crystal detector, using an energy window of 450–570 keV.

2.2. Time pickoff procedure

Fig. 2 shows typical 511 keV dynode signals for both detectors. The 10–90% risetime was ~ 5.3 ns for the LYSO-MAPMT dynode signal and ~ 2.1 ns for the BaF_2 dynode signal.

In all timing-related analysis, the 511 keV full-energy peak was selected in both detectors. Specifically, an energy window of 450–570 and 380–660 keV was applied for the LYSO and BaF_2 events, respectively. This corresponded to 67% of the coincidence events for LYSO and 42% of the coincidence events for BaF_2. Taken together, the timing analysis included 28% of all coincidence events.

As time pickoff procedure, a digital constant fraction (dCF) procedure was used [12]: First, the detector signal was recovered from the sampled waveform by full cubic spline interpolation. Next, a delayed waveform and an attenuated and inverted waveform were created from the interpolated input waveform. The two waveforms were added to form the bipolar dCF signal. Fig. 2 shows typical bipolar dCF signals. The arrival time was determined as the zero-crossing time of the bipolar dCF signal. For the LYSO-MAPMT dynode signal, a delay of 15 ns and an attenuation factor of 0.06 were chosen. For the BaF_2 dynode signal, 3 ns was chosen as delay and 0.18 as attenuation factor. These parameter values gave the optimal coincidence timing resolution. The coincidence timing resolution is deduced from the spectrum of the time differences between the LYSO and BaF_2 signals.

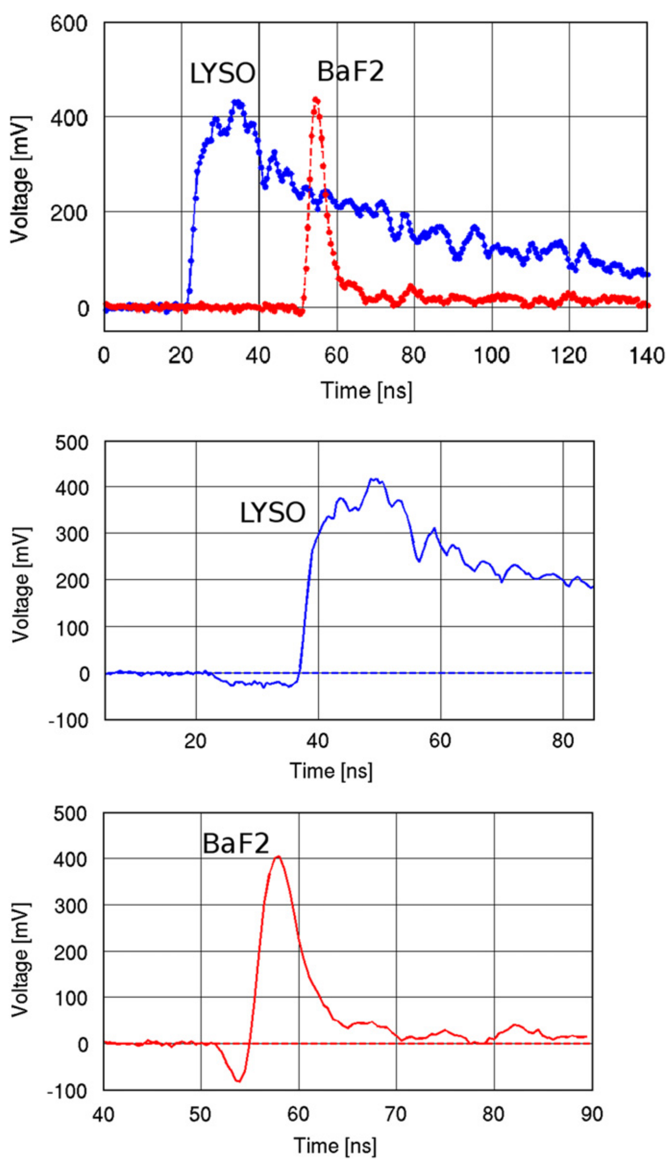

Fig. 2. Upper graph: typical 511 keV LYSO-MAPMT (solid blue line) and BaF_2 (dashed red line) dynode signals. The dots indicate the digitizer sampled points. Lower graphs: Bipolar dCF signals for which the zero-crossing moment defines the pulse time. Middle graph: LYSO-MAPMT dCF signal. Lower graph: BaF_2 dCF signal. (For interpretation of the references to colour in this figure legend, the reader is referred to the web version of this article.)

2.3. Calibration scans

In the following sections, the x- and y-coordinates define the coordinates parallel to the MAPMT plane and range between 0 and 20 mm. The center of the detector is thus located at $(x,y)=(10,10)$. The z-coordinate defines the coordinate perpendicular to the MAPMT plane and ranges between 0 and 12 mm and corresponds to the DOI. The MAPMT plane is located at $z=12$ mm.

Scans of the monolithic crystal were performed with the gamma beam impinging perpendicularly on the 20 mm × 20 mm front face (XY-scan) and on one of the 20 mm × 12 mm side faces (YZ-scan). Both scans were performed with a 2 mm grid spacing. For every beam position 10,000 coincidence events were collected. After selecting the full-energy events for the monolithic crystal detector, ~6,700 events remained per beam position (see Section 2.2). The YZ-scan provides the detector response at defined z-positions and thus allows the estimation of the DOI for the events in the XY-scan. By combining the information from the XY- and YZ-scans, the x-, y- and z-coordinate of the photoconversion position in the crystal can be estimated for any event. The used algorithms are described in Sections 2.4, 2.5 and 2.6.

Because of the exponential attenuation law, the positions of the photon interactions are not uniformly distributed over the crystal. The annihilation photon flux decreases exponentially as a function of DOI (for LYSO the radiation length is 11.6 mm). This implies that the calibration sets contain more events at small DOI than events at large DOI. Specifically, the XY-scan contains more events at small z-coordinates ($z<6$) than events at large z-coordinates ($z>6$). Likewise, the YZ-scan contains more events at small x-coordinates ($x<10$) than events at large x-coordinates ($x>10$).

2.4. 2D-calibration of the XY-scan

For each event, the photon distribution pattern $\{m_1,m_2,\ldots,m_{16}\}$ was calculated by normalizing the MAPMT detected energies e_i by the total detected energy as follows:

$$m_i = e_i \Big/ \sum_{j=1}^{16} e_j \tag{1}$$

here i is the MAPMT anode index. The probability density function of m_i for a certain anode and for a certain beam position is an anode response function (RF). The XY-scan of 11 × 11 grid points thus gives 1936 response functions. Each of these is least-square fitted with a Gaussian with a high-energy exponential tail:

$$RF_i[m_i|x,y] = \begin{cases} N \cdot \exp\left(-\dfrac{(m_i-\mu_i)^2}{2\sigma_i^2}\right) & m_i \le (\mu_i+\Delta_i) \\ N \cdot \exp\left(\dfrac{-\Delta_i \cdot (m_i-\mu_i-\Delta_i/2)}{\sigma_i^2}\right) & \text{otherwise} \end{cases} \tag{2}$$

where N is the normalization constant:

$$N = \frac{1}{\sqrt{\pi/2}\cdot\sigma_i\cdot\left(1+\mathrm{erf}\left(\dfrac{\Delta_i}{\sqrt{2}\sigma_i}\right)\right)+\dfrac{\sigma_i^2}{\Delta_i}\exp\left(-\dfrac{\Delta_i^2}{2\sigma_i^2}\right)} \tag{3}$$

with *erf* the Gauss error function. Thus, for each anode (i) and beam position (x,y), the response function is described by three parameters:

- centroid: $\mu_i(x,y)$,
- width: $\sigma_i(x,y)$,
- start of tail with respect to centroid: $\Delta_i(x,y)$ ($\Delta_i > 0$).

The exponential tail shows up for anodes in line with the gamma beam and results from photoconversion locations near the MAPMT. For these locations a relatively large fraction of scintillation photons accumulates in the nearby anode, resulting in a large value for m_i for the particular anode.

For purely Gaussian functions, the tail parameter attains an asymptotic value: $\Delta_i \to \infty$. To obtain an alternative to this parameter with a limited value range, another variable was introduced in the model: the fraction $f_i(x,y)$ of the peak amplitude of the distribution at which the tail starts; by definition its range is between 0 and 1. Δ_i is related to f_i as follows:

$$\Delta_i = \sigma_i \sqrt{-2\ln(f_i)} \quad (4)$$

Fig. 3 shows an example of a fitted response function with exponential tail.

The values of $\mu_i(x,y)$, $\sigma_i(x,y)$ and $f_i(x,y)$ (as function of beam position and anode index) were stored for further processing in the MLE position estimation. To obtain the parameter values on a fine grid with 0.5 mm spacing (as opposed to the 2 mm grid of the calibration scan), a bicubic spline interpolation was applied. As an example, Fig. 4 shows the centroid distribution for one of the central anodes as a function of beam position.

Given a certain beam position (x,y), the probability for observing the photon distribution pattern $\{m_1,m_2,\ldots,m_{16}\}$ is given by the product of the individual normalized response functions:

$$P[m_1,m_2,\ldots,m_{16}|x,y] = \prod_{i=1}^{16} RF_i[m_i|x,y] \quad (5)$$

The other way around, given a certain pattern $\{m_1,m_2,\ldots,m_{16}\}$, the probability that the pattern was generated by a beam at position (x, y) is given by the same equation. In the MLE-approach, the estimate of beam position, $(\hat{x},\hat{y})$, for a certain pattern $\{m_1,m_2,\ldots,m_{16}\}$ is the one that maximizes this probability:

$$(\hat{x},\hat{y}) = \arg\max_{x,y} P[m_1,m_2,\ldots,m_{16}|x,y] \quad (6)$$

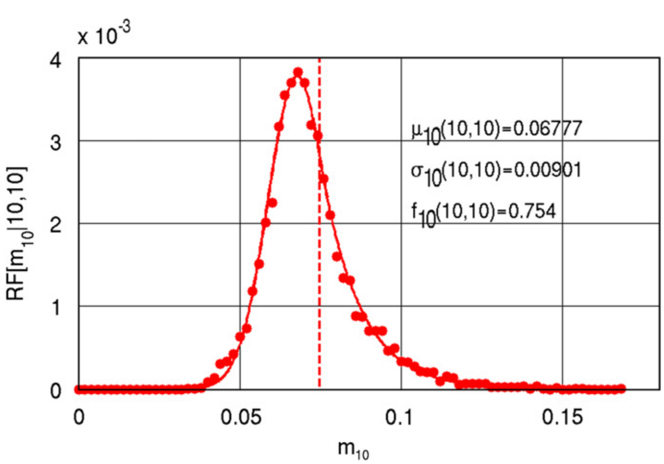

Fig. 3. Fitted response function from the XY-scan for anode #10 and xy-beam position in the center of the crystal: (x,y)=(10,10). The dotted vertical line represents the transition from the Gaussian to exponential regime. The values of the fitted parameters $\mu_i(x,y)$, $\sigma_i(x,y)$ and $f_i(x,y)$ are given.

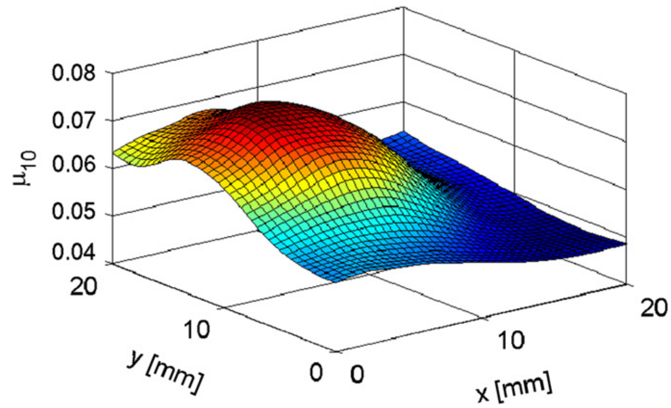

Fig. 4. Centroid distribution for anode #10, $\mu_{10}(x,y)$, as function of beam position on a 0.5 mm grid.

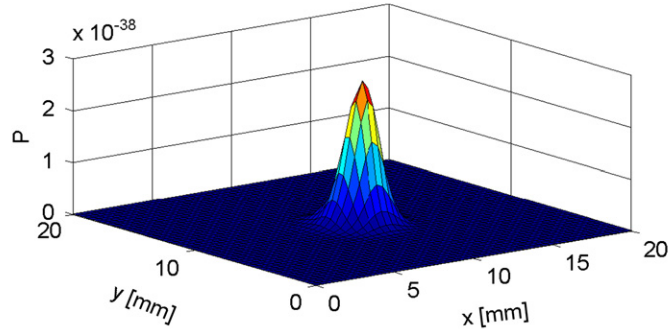

Fig. 5. Distribution of $P[m_1,m_2,\ldots,m_{16}|x,y]$ in the xy-plane for a certain event.

It is noteworthy to explicitly mention here that with this MLE-approach no prior knowledge on the scintillation photon distribution patterns $\{m_1, m_2,\ldots,m_6\}$ is used during the estimation of the position-of-interaction. Additionally, no assumption is made about the variance of the normalized detected anode energy m_i. This variance is captured by the σ_i parameter in Eq. (2) and is thus independently calibrated for each anode as a function of beam position. Determined from experiment, this σ_i parameter inherently contains all variance contributions, such as varying number of generated photons per scintillation event, PMT gain variance, electronic noise, etc. Likewise, the systematic variation of m_i with DOI is captured by the tail parameter f_i and is thus also determined from experiment. The MLE-estimation in Eq. (6) calculates the probability of a beam position for a certain event using the calibration information on signal variance and DOI dependence, along with the calibrated information on the average signal.

Fig. 5 shows the distribution of $P[m_1,m_2,\ldots,m_{16}|x,y]$ for a certain event. The peak value can clearly be localized. For each event, the maximum of the probability distribution was searched on a 0.5 mm grid and the x- and y-position corresponding to this maximum were taken as the estimated x- and y-position of the photoconversion inside the crystal.

2.5. 3D-calibration of the YZ-scan

The calibration method that was used for the XY-scan could not directly be used for the YZ-scan. It was found that anode response functions for which the gamma beam passes close to the MAPMT are heavily distorted from a Gaussian-like shape, making a parametrization of the response function inconvenient. The reason is that the data set for a certain (y,z) position of the gamma beam contains interactions for which the photoconversion x-position covers the whole 20 mm width of the crystal. For a particular anode, this results in a large signal when the photoconversion x-position is close to the anode and a small signal when this position is far away from the anode.

To remedy this, the photoconversion x-position was estimated for each YZ-event using the method described in Section 2.4. A 3D-calibration set was built based on the estimated x-position and the beam-defined y- and z-position. Thus a separate response function was constructed for each of the 16 anodes, each of the 11×7 (y,z) grid positions of the incoming gamma beam and each of the (chosen) 10 bins of 2 mm width in the x-direction, giving a total of 12,320 response functions. For these response functions, the Gaussian with exponential tail appeared to be a reasonable model and the procedure detailed in Section 2.4 to determine the three parameters $\mu_i(x,y,z)$, $\sigma_i(x,y,z)$ and $f_i(x,y,z)$ was performed. An example of a response function is shown in Fig. 6. Here the photoconversion position was chosen near the MAPMT: $(x,y,z)=(10,10,10)$ (the MAPMT is located at $z=12$). Note the higher centroid value compared to the one in Fig. 3 with $(x, y)=(10,10)$ for which the z-coordinate covered the full thickness of the crystal. This is evidently caused by a larger scintillation photon flux at the anode location due to the nearby photoconversion position.

To obtain the parameter values on a fine 3D-grid with 0.5 mm spacing, a tricubic spline interpolation was applied. For an event, the 3D-photoconversion position could now be estimated using a 3D-version of the MLE estimation method:

$$(\hat{x},\hat{y},\hat{z}) = \arg\max_{x,y,z} P[m_1,m_2,\ldots,m_{16}|x,y,z] \qquad (7)$$

2.6. 3D-calibration of the XY-scan

When building a 3D-calibration set according to the method in the previous section, the set will be built from events in the YZ-scan. The 2D-calibration set in Section 2.4 is built from events in the XY-scan. In order to be able to make a direct comparison in x- and y-position reconstruction performance between a 2D-MLE and 3D-MLE set, it is desirable that the 3D-calibration set is also built from events in the XY-scan. In this way, in case a performance difference is observed, one can exclude the possibility that this is caused by differences in the distribution of photoconversion positions in the XY- and YZ-calibration set.

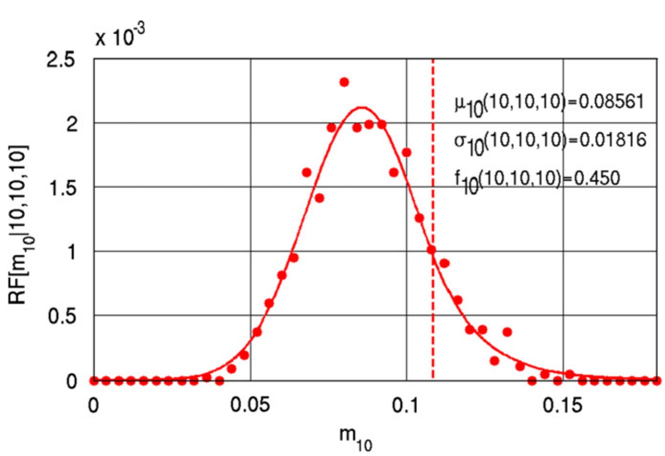

Fig. 6. Fitted response function from the YZ-scan for anode #10, yz-beam position $(y,z)=(10,10)$, and for which the gamma photons interacted in the x-position range $9\le x\le 11$. The dotted vertical line represents the transition from the Gaussian to exponential regime. The values of the fitted parameters $\mu_i(x,y,z)$, $\sigma_i(x,y,z)$ and $f_i(x,y,z)$ are given.

(The position of the photon interaction is not uniformly distributed over the crystal, see Section 2.3). When both the 2D-MLE and 3D-MLE calibration sets are based on events from the XY-scan, the calibrated information density as function of position (i.e. number of photoconversion interactions as function of position) is exactly the same for both sets. In order to obtain a 3D-calibration set from events in the XY-scan, the photoconversion z-position was estimated for each XY-event using the method described in Section 2.5. Specifically, the 3D-calibration set built from YZ-events was used to estimate the photoconversion z-position, by searching the maximum probability on the 3D-grid in Eq. (7). A new 3D-calibration set was built based on the estimated z-position and the beam-defined x- and y-position. A separate response function was constructed for each of the 16 anodes, each of the 11×11 (x,y) grid positions of the incoming gamma beam and each of the (chosen) 6 bins of 2 mm width in z-direction, giving a total of 11,616 response functions. For the remainder of the calibration procedure and the MLE estimation method, the same procedure was followed as outlined in Section 2.5.

2.7. MAPMT response characterization

As the characterization of the time walk as a function of scintillation location is a central theme in this paper, it is important to characterize the response of the MAPMT. Differences in transit time, quantum efficiency or gain of the MAPMT anodes would directly affect the time walk measurements. For this purpose, the MAPMT was directly excited by picosecond laser pulses (using a Hamamatsu PLP-10 light pulser) with 405 nm wavelength and 70 ps pulse width. Each MAPMT anode was separately illuminated, covering the other 15 anodes with black tape and ensuring that each illuminated anode had the same position with respect to the laser beam. No attenuation filter was used, to ensure that for each light pulse a large number of light photons were detected in order to minimize the MAPMT transit time spread for an individual anode. (The transit time spread is inversely proportional to the square root of the number of detected photoelectrons [14]). For each anode measurement, digital time pickoff was performed on the dynode signal and the picosecond laser trigger pulse. The time differences were histogrammed and fitted with a Gaussian. The centroids of the time difference spectra were recorded and served as a measure for the relative transit time differences among the anodes. In addition, the energies of the dynode signals were determined by a digital summing operation along the time-axis. The dynode energies were also histogrammed and fitted with a Gaussian. The centroids of the energy histograms served as a measure for the combined effect of anode quantum efficiency and gain.

3. Results and discussion

3.1. Coincidence timing

Fig. 7 shows the time difference spectrum (LYSO minus BaF_2 arrival time) for events from the XY-scan constructed as described in Section 2.2. A coincidence timing resolution of 358 $\pm$0.5 ps FWHM is obtained. The coincidence timing resolutions for the central and middle region (region 1 and 2 in Fig. 13) are both equal to 354 ps FWHM. At the crystal edges (region 3 in Fig. 13) the coincidence timing resolution is somewhat worse: 360 ps FWHM.

Subtracting the contribution from the BaF_2 detector (about 180 ps FWHM) gives a single detector timing resolution of the LYSO detector of about 309 ps FWHM (and a corresponding

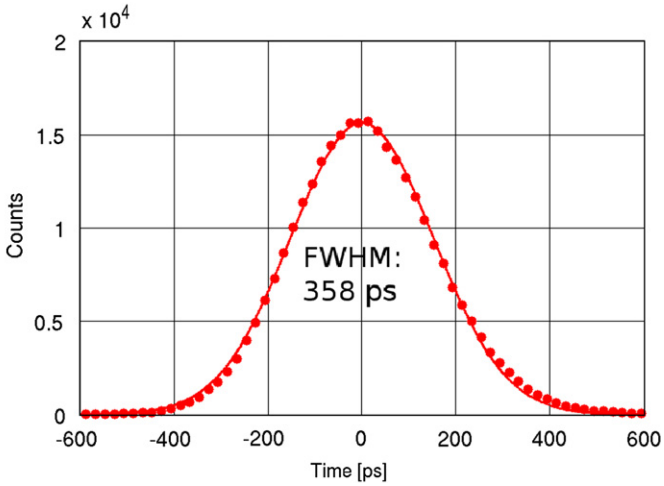

Fig. 7. Time difference spectrum (LYSO minus BaF_2 arrival time) for events from the XY-scan. The centroid is set at 0.

coincidence timing resolution for two such detectors of about 438 ps FWHM).

3.2. *xy*-estimation

Fig. 8 shows the results of the *xy*-reconstruction for three beam positions in the XY-scan as determined using the 2D-MLE and 3D-MLE procedures outlined in Sections 2.4 and 2.6. In the center of the crystal the two estimation procedures have similar performance and a FWHM resolution of ~ 2.4 mm is obtained. At the crystal edges a non-linearity can be observed for the response of the 2D-MLE procedure: the centroid of the reconstructed positions is shifted with respect to the true beam position. Because this does not (or to a far lesser extent) show up for the 3D-MLE response, the effect can evidently be explained by the inability of the 2D-MLE procedure to handle events near the edge of the crystal for which the photoconversion *z*-position (or DOI) covers the whole range of the crystal. At the crystal edges a large fraction of the events have estimated position values in the last bin of the position grid for both procedures. This can be explained by the method of position reconstruction: the MLE-maximum is located on a finite grid spanning the crystal geometry. For events with actual MLE-maxima outside the used grid of reconstruction, the position is estimated on the edges of the grid because the actual MLE-maxima are not covered by the calibrations scans. (Because of the finite position resolution, some MLE-maxima can be located outside the used grid of reconstruction).

As the DOI is simultaneously estimated for the 3D-MLE procedure when reconstructing the *x* and *y* positions, it is possible to evaluate the *xy*-position resolution as function of DOI. In order to do this, 6 DOI-bins of 2 mm width were set up. Individual reconstruction results were assigned to the proper bin, according to the estimated DOI. Because the 3D-MLE procedure has a good linearity performance (see Fig. 8), reconstructions at multiple *xy*-beam positions could be merged to build up statistics. For this purpose, the reconstructed profiles for the *xy*-beam positions in the central 10 mm $\times$ 10 mm square (25 beam positions) were aligned and merged. The resulting FWHM position resolution as function of DOI is shown in Fig. 9. It is apparent that the position resolution improves when the gamma photon interaction position approaches the photosensor. In combination with the exponential attenuation law for gamma photons, this explains the general observation that the position resolution is better when a light sensor is placed at the side of the crystal facing the beam instead of at the opposite side [5,13]. A practical consideration in this respect is the absorption of the gamma photons by the light sensor. This prohibits positioning a PMT on the crystal side facing the beam, but is not an issue for thin semiconductor light sensors.

3.3. *z*-estimation

Since the YZ-scan provides the detector response at defined *z*-positions, it is possible to evaluate the *z*-reconstruction performance of the detector by estimating the position-of-interaction for the events from the YZ-scan. Fig. 10 shows the *z*-resolution for events in the YZ-scan in three regions of the crystal. For locating the MLE-maxima in Eq. (7), 3D-localization was applied using the 3D-calibration set built from the YZ-scan. The FWHM *z*-resolution is about 2.3 mm for events near the sensor array (high *z*-coordinate) and degrades to about 4 mm for events away from the sensor array. The effect of events being attributed to the edge of the crystal as seen in Fig. 8 also shows up here. For events near the sensor array (high *z*-coordinate) a systematic error in the *z*-estimation is present. Sorting the *z*-reconstructions according to the estimated *x*-coordinate, it appeared that this systematic error showed up for events at small *x*-coordinates. Apparently there was a systematic error in the 3D-YZ calibration set for events that interacted in this region. It might have been caused by systematic errors in the *x*-estimation at high *z*-coordinates by the 2D-MLE procedure that was used to build up the 3D-YZ calibration set (see Section 2.5). Fig. 8 also showed that the 2D-MLE procedure had difficulty handling events near the edge of the crystal.

For events from the XY-scan, average photon distribution patterns as a function of the reconstructed *z*-position (i.e. DOI) were set up. This was done by sorting the events from each *xy*-beam position into 6 DOI-bins of 2 mm width according to the reconstructed DOI. The DOI was reconstructed by locating the MLE-maxima in Eq. (7), applying 3D-localization using the 3D-calibration set built from the YZ-scan. For each *xy*-beam position, each DOI-bin and each anode, the m_i distribution (see Section 2.4) was fitted by a Gaussian and the resulting centroid $\overline{m}_i$ was recorded. $\{\overline{m}_1, \overline{m}_2, \ldots, \overline{m}_{16}\}$ thus represented the average scintillation photon distribution pattern. Fig. 11 shows the calculated patterns for 4 *xy*-beam positions at small DOI (DOI = 3 mm) and large DOI (DOI = 11 mm). The patterns show the expected behavior: for positions-of-interaction near the MAPMT (i.e. large DOI), there is a high local flux of scintillation photons at the nearby anode location, resulting in a peaked distribution. This flux is more uniform over the MAPMT when the position-of-interaction is at a larger distance from the MAPMT (i.e. small DOI), resulting in a more uniform distribution. No prior knowledge on the scintillation photon distribution patterns was used during the estimation of the DOI (see Sections 2.4 and 2.5). It demonstrates that the DOI is correlated with the scintillation photon distribution width at the sensor array, even in the presence of a reflective Spectralon enclosure (Section 2.1).

These results show that monolithic scintillation crystals are suitable for accurate DOI-reconstruction using only one photosensor array. A block detector composed of crystal segments is not able to do this directly, since it confines the scintillation light to a single crystal segment and thus the correlation between DOI and scintillation photon distribution width at the sensor array is lost.

Extrapolating the DOI reconstruction result in Fig. 10 to thicker monolithic scintillation crystals coupled to a single photosensor array, we expect that DOI reconstruction is possible for gamma interactions located at a distance of at least 20 mm from the photosensor array.

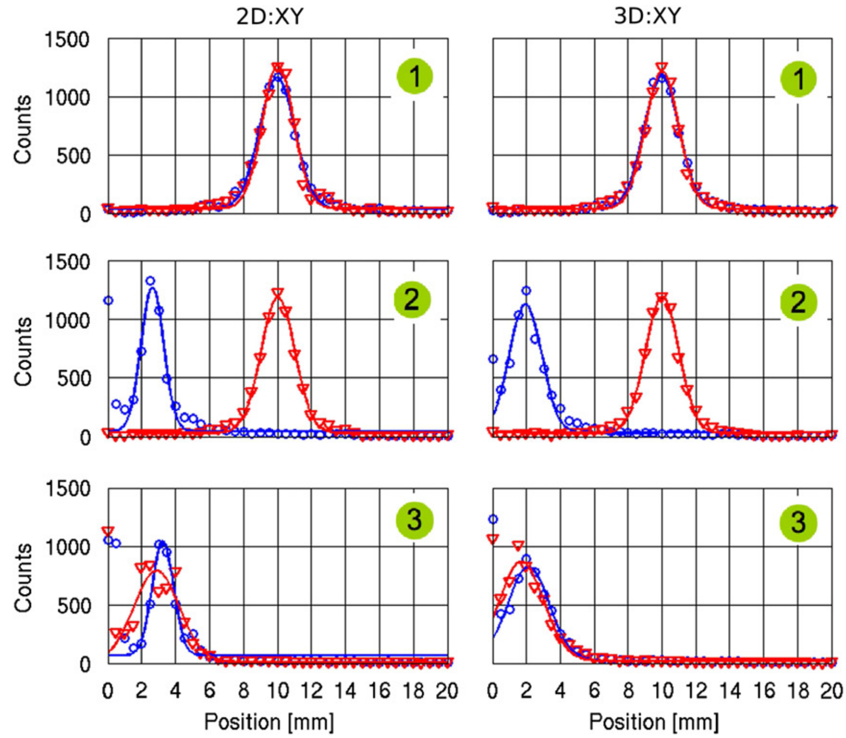

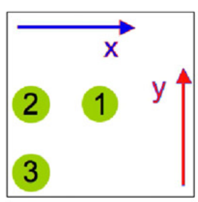

2D:XY			
Beam mark	Beam pos (x,y) [mm]	Centroid (x,y) [mm]	FWHM (x,y) [mm]
1	(10,10)	10.0, 10.0	2.4, 2.2
2	(2,10)	2.6, 10.0	1.6, 2.3
3	(2,2)	3.3, 2.9	1.5, 3.2

3D:XY			
Beam mark	Beam pos (x,y) [mm]	Centroid (x,y) [mm]	FWHM (x,y) [mm]
1	(10,10)	10.0, 10.0	2.4, 2.3
2	(2,10)	1.9, 10.0	2.3, 2.3
3	(2,2)	2.1, 1.7	2.9, 3.1

Fig. 8. Reconstructed *x*-profiles (blue circles) and *y*-profiles (red triangles) for three beam positions in the XY-scan: $(x,y)=(10,10)$; (2,10); (2,2). 2D:XY indicates the 2D-MLE procedure described in Section 2.4; 3D:XY indicates the 3D-MLE procedure in Section 2.6. The values of the centroid and FWHM of the reconstructed position distribution are obtained from a least-square fit with a Gaussian plus constant background (blue(x) and red(y) solid curves). (For interpretation of the references to colour in this figure legend, the reader is referred to the web version of this article.)

3.4. Arrival time versus DOI

Sorting the events from the XY-scan according to the reconstructed DOI (as in Section 3.3) allows the evaluation of the arrival time as a function of DOI. The average arrival time was calculated by fitting the time difference (LYSO time minus BaF_2 time) spectrum by a Gaussian and recording the centroid. The LYSO and BaF_2 times were determined by the time pickoff method in Section 2.2. Fig. 12 shows the result for the three crystal regions shown in Fig. 13.

One observes a time walk vs. DOI, but the walk behavior is not uniform across the crystal. For the central region, events at large DOI are detected earlier than events at small DOI (the LYSO minus the BaF_2 arrival time is smaller). For the middle region in Fig. 13, the time walk is less apparent; for the edge region, events at large DOI are detected at a later time than events at small DOI.

Fig. 14 provides some insight into this complex walk behavior. For each event, the dynode energy was calculated from the digitized MAPMT dynode waveforms (shown in Fig. 2) by a digital summing operation along the time axis. Events from the XY-scan were sorted into $2\times 2\times 2\,\mathrm{mm}^3$ voxels according to the beam-defined *x*- and *y*-position and the reconstructed DOI. For each voxel, Gaussian fits of the dynode energy distribution and the time difference distribution were performed. The energy and time centroids are shown in Fig. 14 for the *z*-planes at large DOI (9 mm) and small DOI (3 mm). Note that the time walk graphs in Fig. 14 show the same behavior as the time walk graph in Fig. 12. It is apparent that the average dynode energy shows the same pattern over position as the time walk and that these two quantities are thus somehow related.

It has to be checked whether the constant fraction time pickoff algorithm (Section 2.2) was able to correct for time walk induced by pulse amplitude variation. (Since the pulse amplitude is determined by the dynode energy, this might be a possible explanation for the observed relationship between time walk and dynode energy). This can be done by selecting a crystal region for which there is no time walk variation over position, and verifying that the average arrival time over dynode energy is constant in this region. In Figs. 12 and 14 one observes that there is almost no time walk over *xy*-position for the crystal region at small DOI. Although the average dynode energy is also constant in this region (Fig. 14), this does not imply that there is no variation in dynode energy over the events: The FWHM of the LYSO dynode energy resolution is equal to 11.4%, which is normal for LYSO at 511 keV. This variation in LYSO dynode energy at small DOI covers the full range of the variation in *average* LYSO dynode energy over the entire crystal shown in Fig. 14. Fig. 15 shows the arrival time variation over dynode energy at small DOI ($0.5 \leq \text{DOI} \leq 1.5$ mm). It is apparent that there is virtually no time walk over dynode energy in this region, as desired from the time pickoff algorithm. The correlation between the average dynode energy and the time walk in Fig. 14 can thus not be attributed to the time pickoff algorithm.

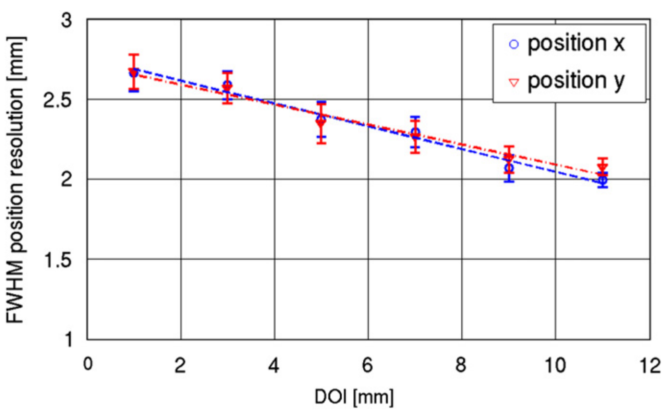

Fig. 9. FWHM position resolution of the 3D-MLE reconstruction as function of DOI for *xy*-beam positions in the central 10 mm × 10 mm square of the crystal. The error bars indicate the 95%-confidence bounds for the FWHM resolution, as obtained from a least-square fit with a Gaussian plus constant background. The lines show the result of a linear fit. The MAPMT is located at $z=12$ mm.

A potential cause for the time walk and dynode energy variation over position might be a non-uniformity in the response between the MAPMT anodes. The MAPMT response was characterized according to the method in Section 2.7. The energy and time centroids vary randomly over the anodes, no pattern can be discerned. The dynode energy and arrival time patterns observed in Fig. 14 can thus not be attributed to the anode non-uniformity of the MAPMT. At large DOI the largest fraction of the scintillation light is collected by the center anodes for events from the center region (see Fig. 11). The same holds for the edge anodes for events from the edge region. By averaging the centroids of the time difference spectra over the four center anodes and the 12 edge anodes separately, it appeared that the center anodes reacted on average about 20 ps faster than the edge anodes. For the LYSO crystal, there was a variation in the average arrival time at large DOI (DOI = 11 mm) of ~ 100 ps between events from the center and edge region (see Fig. 12). This also means that the arrival time variation at large DOI can not be attributed to the anode non-uniformity of the MAPMT.

When one excludes the possibility that the dynode energy variation over position is caused by a non-uniformity in the response between the MAPMT anodes, the variation can only be caused by a varying scintillation light loss over position. This implies that for scintillation locations at large DOI nearby the crystal side surfaces the largest number of scintillation photons is lost (see Fig. 14); for scintillation locations at large DOI in the center of the crystal the smallest number of scintillation photons is lost; while at small DOI the loss is more uniform vs. *x*,*y* position and in between these two extremes. Likewise, when one excludes that the time walk variation over position is caused by a

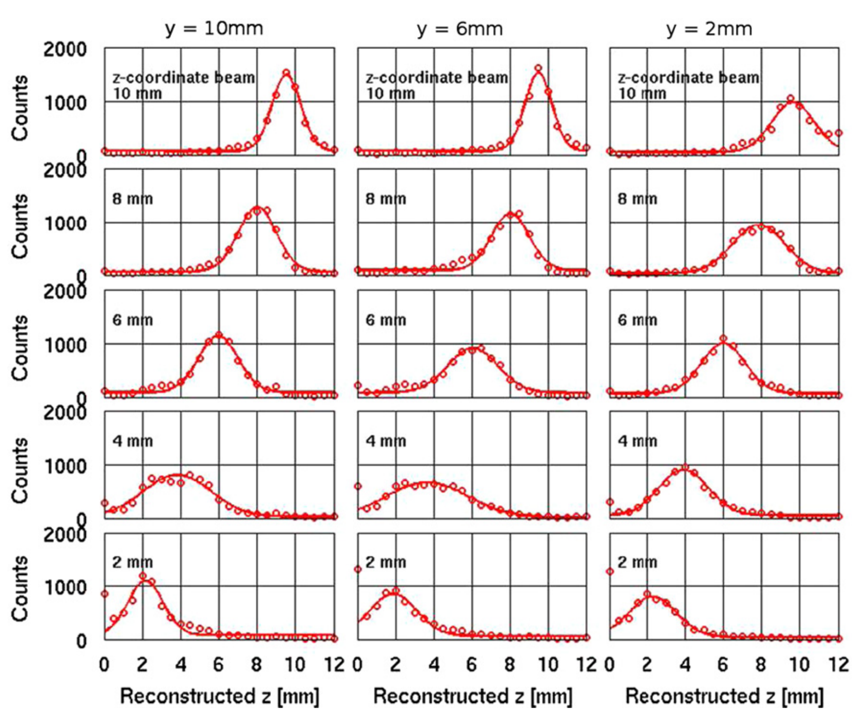

Fig. 10. *z*-resolutions for YZ beam positions in the center ($y=10$ mm), off center ($y=6$ mm) and edge ($y=2$ mm) of the crystal. The MAPMT is located at $z=12$ mm.

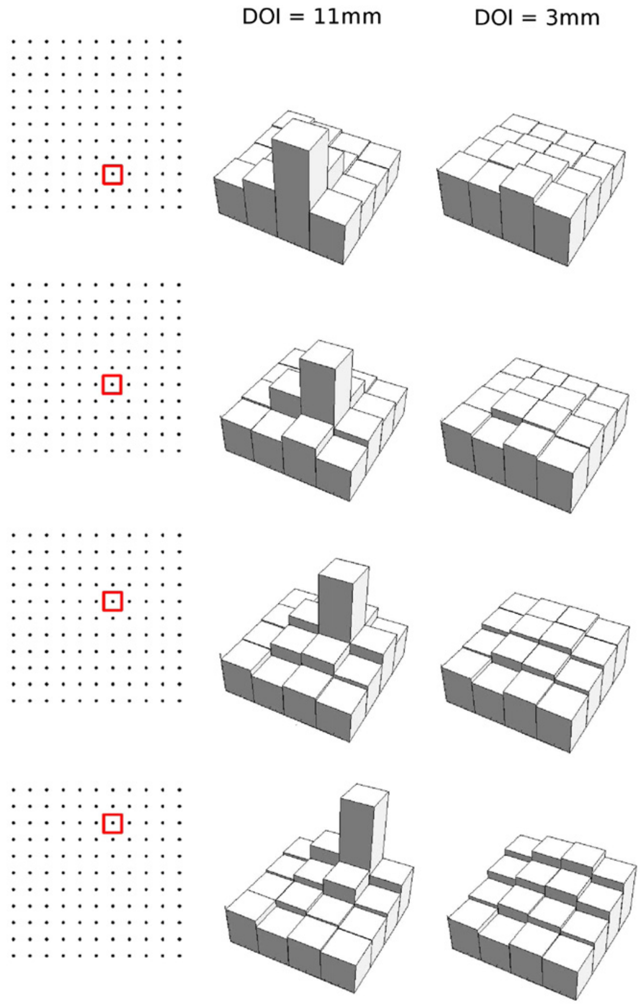

Fig. 11. Average scintillation photon distribution patterns $\{\overline{m}_1, \overline{m}_2, \ldots, \overline{m}_{16}\}$. The left column indicates *xy*-beam positions for which the $\{\overline{m}_1, \overline{m}_2, \ldots, \overline{m}_{16}\}$ patterns are shown at $10 \le \mathrm{DOI} \le 12$ mm (center column) and $2 \le \mathrm{DOI} \le 4$ mm (right column).

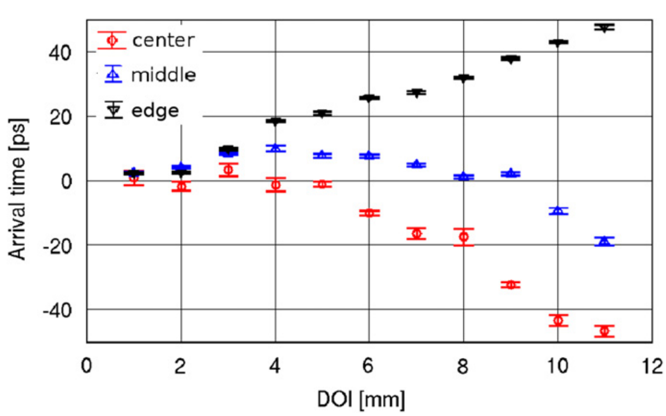

Fig. 12. Fitted centroid of the time difference spectra (LYSO minus BaF_2 arrival time) as a function of DOI for XY-beam positions in the three crystal regions shown in Fig. 13. The error bars indicate the 95%-confidence bounds. The MAPMT is located at DOI = 12 mm.

non-uniformity in the response between the MAPMT anodes, the variation can only be caused by a variation in travel time of the scintillation photons from their point of creation to the photosensor.

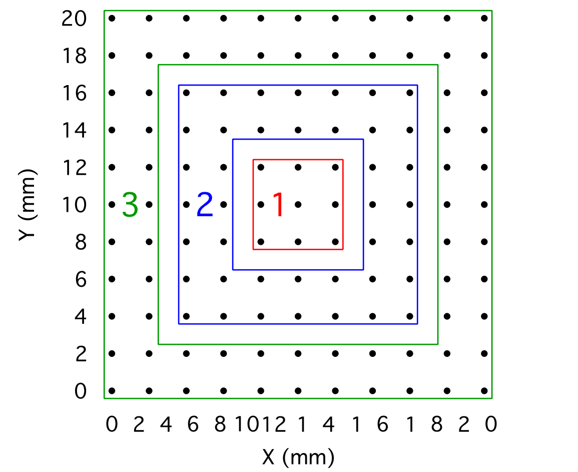

Fig. 13. Regions selected in the XY-scan for analysis of the DOI time walk effect (Fig. 12): center (1); middle (2); edge (3). The dots represent the calibration scan grid.

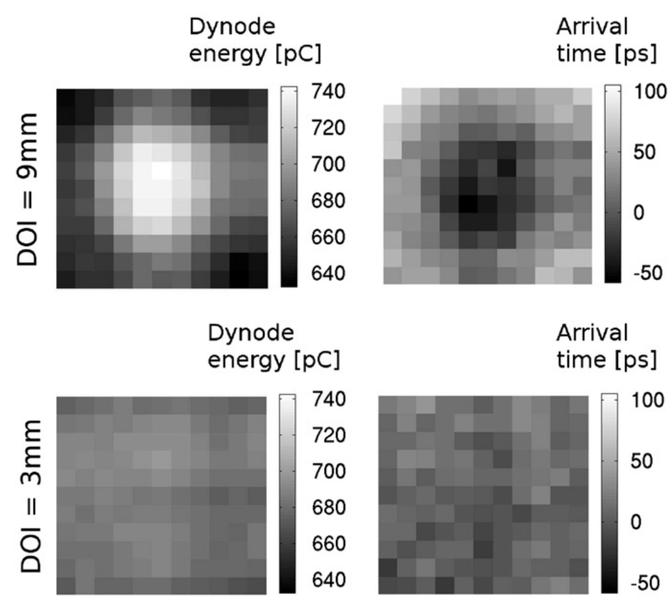

Fig. 14. Dynode energy distribution and arrival time distribution in the transversal *xy*-planes located at large DOI ($8 \le \mathrm{DOI} \le 10$ mm) and small DOI ($2 \le \mathrm{DOI} \le 4$ mm). Each *xy*-bin corresponds to a beam position in the scan grid (Fig. 13).

Photon loss is to be attributed to self-absorption inside the crystal and absorption at the surfaces, and as such depends on the scintillator material quality, the surface finish and the packaging. Reflection at the surfaces is on average accompanied by a longer travel path and thus longer travel time as well as larger self-absorption. The observed time walk behavior thus results from differences in the scintillation photon transport from the place of creation to the sensor.

Light collection is slower towards the edges/corners due to the increased importance, because of geometric reasons, of reflections with the crystal surfaces. This effect is enhanced at large DOI because the crystal surface coupled to the MAPMT ($20 \times 20\,\mathrm{mm}^2$) is somewhat larger than the sensitive area of the MAPMT ($18 \times 18\,\mathrm{mm}^2$). The time walk is reduced for small DOI because of the vicinity of the crystal front edge which reflects scintillation photons that were emitted away from the MAPMT, increasing the early photon flux towards the MAPMT, i.e. speeding up the arrival

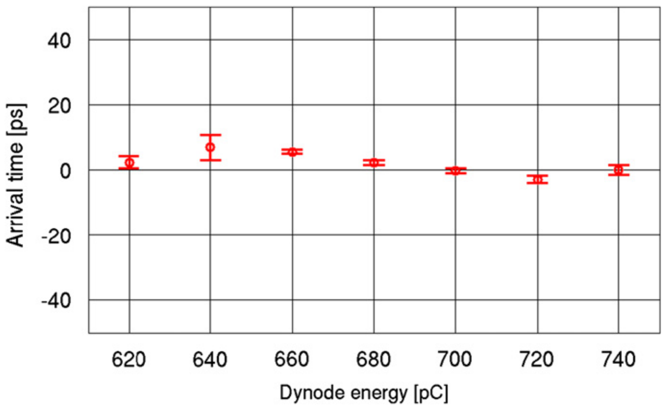

Fig. 15. Fitted centroid of the time difference spectra (LYSO minus BaF_2 arrival time) as a function of the dynode energy in 20 pC bins for the transversal *xy*-plane located at small DOI ($0.5 \leq \mathrm{DOI} \leq 1.5$ mm). The error bars indicate the 95% confidence bounds.

Table 1
Coincidence resolving times (CRTs) for different DOI regions. The third column indicates the obtained CRTs after performing a position correction to the timing. The fourth column indicates the improvement in CRT due to this correction.

DOI region (mm)	FWHM CRT without correction (ps)	FWHM CRT with correction (ps)	CRT improvement (ps)
[0–12]	357.7 ± 0.5	353.5 ± 0.5	4.2
[6–12]	360.4 ± 0.5	352.5 ± 0.5	7.9
[9–12]	364.8 ± 0.8	352.6 ± 0.7	12.2
[10.5–12]	368.0 ± 1.1	351.7 ± 0.9	16.3

of the first few photons, and thus counteracting the time walk with DOI. The speed of scintillation photons within the crystal is equal to c/n (with c the speed of light in vacuum and n the index of refraction, about 1.82 for LYSO). The maximum average arrival time variation of ~100 ps in Fig. 12 translates into an average path length variation of ~16 mm, not surprisingly comparable to the crystal size.

Using the observed time walk vs. 3D gamma interaction position, an event-by-event software correction to the timing can be applied. After correction, the residual time walk throughout the crystal is at the level of just a few ps. For the detector used in this work, only a small improvement of the overall coincidence timing resolution from 358 to 354 ps FWHM results (see Table 1), since most gamma photons interact at small DOI, where time walk is small. When only taking events at large DOI into account, the improvement is larger (see Table 1).

For $3 \times 3 \times 30\,\mathrm{mm}^3$ LSO crystals Moses and Derenzo reported arrival time variations between 200 and 400 ps, depending on the crystal surface treatment [15]. It was shown that this effect significantly degraded the timing resolution for detectors utilizing these crystals. They attributed the effect to the scintillation light undergoing multiple reflections at quasi-random angles within the crystal.

The crystal thickness in the current work was equal to 12 mm. For thicker monolithic crystals one expects a larger arrival time variation, thereby degrading the timing resolution. A time walk correction according to the estimated interaction position may improve the timing resolution for such crystals.

4. Conclusion

In order to investigate the time walk as function of photoconversion location inside a monolithic crystal coupled to a photosensor array, a maximum likelihood estimation algorithm that determines the x-, y-, and z (i.e. DOI)-coordinates of the photoconversion location was developed. For a $20\,\mathrm{mm} \times 20\,\mathrm{mm} \times 12\,\mathrm{mm}$ LYSO crystal coupled to a fast 4×4 multi-anode photomultiplier tube, a spatial resolution in the plane of the MAPMT of 2.4 mm FWHM is obtained. The DOI-resolution ranges from 2.3 mm FWHM near the photomultiplier tube to 4 mm FWHM at a distance of 10 mm. These resolutions are uncorrected for the ~1 mm diameter beam of annihilation photons. In a coincidence setup with a BaF_2 detector, timing signals were digitized at 2 GS/s and digital time pickoff was performed. A coincidence timing resolution of 358 ps FWHM was obtained. A time walk depending on the 3D photoconversion location is observed. The time walk throughout the crystal spans a range of 100 ps. Calibrating the time walk vs. interaction location allows an event-by-event correction that leaves a residual time walk of just a few ps, making it irrelevant for the timing performance of the detector. From an extrapolation of our results, we estimate that the DOI resolution is sufficient to correct for time walk such that it becomes irrelevant up to a crystal thickness of at least 20 mm, thick enough for an L(Y)SO-based PET scanner. The same can hold for even thicker crystals when using a photosensor array at both the front and back. This geometry is possible with solid-state sensors such as silicon photomultipliers, and is especially relevant for $LaBr_3$ crystals as the rather large 511 keV attenuation length of 22 mm warrants the use of thick crystals.

References

[1] D.J. van der Laan, M.C. Maas, H.W.A.M. de Jong, D.R. Schaart, P. Bruyndonckx, C. Lematre, C.W.E. van Eijk, Nucl. Instr. and Meth. Phys. Res. A 571 (2007) 227.
[2] P. Bruyndonckx, C. Lemaitre, D. Schaart, M. Maas, D.J. van der Laan, M. Krieguer, O. Devroede, S. Tavernier, Nucl. Instr. and Meth. A 571 (2007) 182.
[3] S. Tavernier, P. Bruyndonckx, S. Leonard, O. Devroede, Nucl. Instr. and Meth. A 537 (2005) 321.
[4] M.C. Maas, D.R. Schaart, D.J. van der Laan, P. Bruyndonckx, C. Lemaitre, F.J. Beekman, C.W.E. van Eijk, Phys. Med. Biol. 54 (2009) 1893.
[5] D.R. Schaart, H.T. van Dam, S. Seifert, R. Vinke, P. Dendooven, H. Lohner, F.J. Beekman, Phys. Med. Biol. 54 (2009) 3501.
[6] J. Joung, R.S. Miyaoka, T.K. Lewellen, Nucl. Instr. and Meth. A 489 (2002) 584.
[7] T. Ling, T.H. Burnett, T.K. Lewellen, R.S. Miyaoka, Phys. Med. Biol. 53 (2008) 1843.
[8] W.W. Moses, IEEE Trans. Nucl. Sci. NS-50 (2003) 1325.
[9] J.S. Karp, S. Surti, M.E. Daube-Witherspoon, G. Muehllehner, J. Nucl. Med. 49 (2008) 462.
[10] Dow Corning Corporation, 〈www.dowcorning.com〉.
[11] Labsphere Corporation 〈http://www.labsphere.com/〉.
[12] G.F. Knoll, Radiation Detection and Measurement, Wiley, New York, 2000.
[13] M.C. Maas, D.J. van der Laan, D.R. Schaart, J. Huizenga, J.C. Brouwer, P. Bruyndonckx, S. Leonard, C. Lemaitre, C.W.E. van Eijk, IEEE Trans. Nucl. Sci. NS-53 (2006) 1071.
[14] Hamamatsu Photonics K.K., Photomultiplier Tubes: Basics and Applications, Edition 3a.
[15] W.W. Moses, S.E. Derenzo, IEEE Trans. Nucl. Sci. NS-46 (1999) 474.